

A leaping, triggered sequence along a segmented fault: The 1951 M_L 7.3 Hualien-Taitung earthquake sequence in eastern Taiwan

Kate Huihsuan Chen,¹ Shinji Toda,² and Ruey-Juin Rau¹

Received 14 March 2007; revised 8 October 2007; accepted 30 November 2007; published 16 February 2008.

[1] As the most destructive seismic episode ever known in eastern Taiwan, the 1951 M_L 7.3 Hualien – Taitung earthquake series consisted of sequential ruptures along four distinct fault segments. It provides a good opportunity to study earthquake triggering processes along an active fault at an oblique arc-continent collision boundary. This sequence initiated on 21 October 1951 with the M_L 7.3 Hualien main shock and a group of M_6+ aftershocks nearby. The M_L 6.0 Chihshang earthquake occurred 34 days later and 100 km away from the main shock. The M_L 7.3 Yuli earthquake followed 3 m later and 5 km away from the Chihshang event. Two days later, the M_L 6.0 Taitung earthquake shocked a region 40 km away from the preceding M_6 event and completed the sequence. The first triggered rupture outside the main shock area did not occur on the nearby Yuli fault segment but occurred 100 km away at the Chihshang fault. Calculations of static Coulomb stress change show that most of the major aftershocks were located in areas of enhanced static stress change. However, the stress transfer alone cannot explain triggering across 100 km. With the rate/state stress transfer model, we computed the temporal order of encouraged ruptures on different segments along the collision boundary. The results show that 34 days following the major shocks in Hualien, the Chihshang segment had a higher M_6+ ($M \geq 6$) earthquake probability due to its significantly higher (at least an order of magnitude) background seismicity rate than the other two segments. After the Chihshang event, the rate/state model predicted a higher M_6+ earthquake probability in the Yuli segment, also matching the observation. In this case, the Yuli segment was triggered ahead of the Taitung segment because of its larger increase in Coulomb stress change.

Citation: Chen, K. H., S. Toda, and R. -J. Rau (2008), A leaping, triggered sequence along a segmented fault: The 1951 M_L 7.3 Hualien-Taitung earthquake sequence in eastern Taiwan, *J. Geophys. Res.*, 113, B02304, doi:10.1029/2007JB005048.

1. Introduction

[2] In 1951, a large earthquake sequence shocked eastern Taiwan from 21 October to 5 December. The 1951 M_L 7.3 Hualien-Taitung earthquake sequence (H–T sequence), composed of twelve $M \geq 6$ events, is the most destructive episode ever recorded in eastern Taiwan [Gutenberg and Richter, 1954; Lee *et al.*, 1978; Abe, 1981; Hsu, 1985; Cheng *et al.*, 1996]. It occurred along the segmented 150-km-long Longitudinal Valley fault (LVF), and was composed of the reverse and strike-slip events that ruptured four segments. The M_L 7.3 main shock occurred near Hualien at 21:34 (GMT) on 21 October 1951 and created a surface rupture on the Meilun fault in the northern end of the LVF. Several hours after the main shock, two other M_L 7 events occurred in the same area (Events 2 and 5 in Figure 1 and Table 1). One month later, on 24 November, two major

earthquakes struck the middle part of the LVF. They occurred just 3 m apart and broke two different surface faults, the Chihshang fault and the Yuli fault. The first M_L 6.0 event on the Chihshang fault was located ~100 km away from the main shock and 5 km south of the second M_L 7.3 event on the Yuli fault [Hsu, 1962; Cheng *et al.*, 1996]. Thirty-six days after the main shock, the last major earthquake occurred in the southern end of the LVF at Taitung, with $M_L = 6.0$. Overall, the 1951 H–T sequence is characterized by a leaping behavior, that is, the first fault ruptured in the north end, the second ruptured 100-km away from the main shock in the southern segment, the third ruptured in the middle segment, and the last occurred again in the southern end of the LVF [Taiwan Weather Bureau, 1952]. The sequential surface ruptures of the Hualien, Chihshang, Yuli segments, and the major events on the Taitung segment reported by Hsu [1962] are shown in Figure 1. Here we seek to understand how segmented faults react to nearby large earthquakes, and why the subsequent events did not rupture the nearest fault first.

[3] The LVF is an active arc-continent collision boundary between the Philippine Sea plate and Eurasian plate. It has been characterized as an active reverse fault with a left-

¹Department of Earth Sciences, National Cheng Kung University, Tainan, Taiwan.

²Active Fault Research Center, Geological Survey of Japan, National Institute of Advanced Industrial Science and Technology, Tsukuba, Japan.

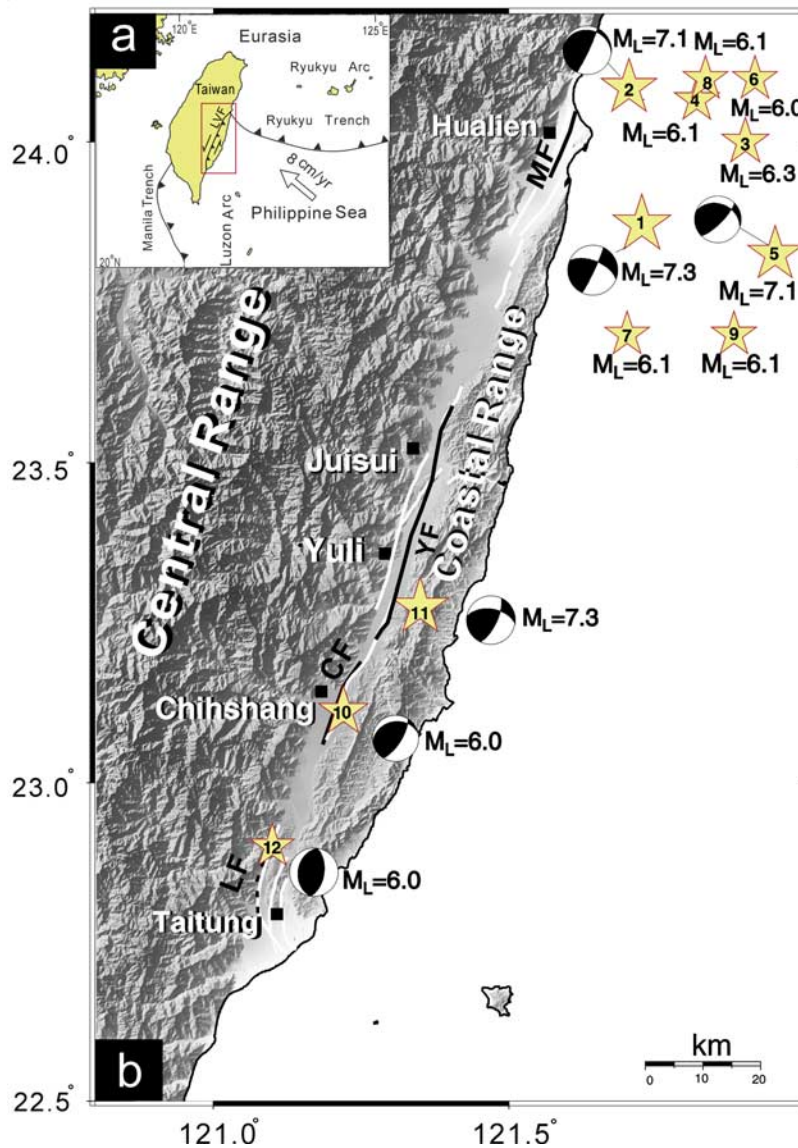


Figure 1. (a) Geodynamic framework of Taiwan. (b) Temporal and spatial distribution of major earthquakes (stars) during the 1951 H–T earthquake sequence in eastern Taiwan. Number in the star corresponds to the ID number listed in Table 1. Focal mechanisms were determined by *Cheng et al.* [1996] and are shown in Table 2. White lines indicate the current active faults, and bold black lines indicate surface ruptures of the 1951 H–T earthquake sequence. Dashed line in the south indicates the non-ruptured fault segment during 1951 sequence. MF, Meilun fault; YF: Yuli fault; CF, Chihshang fault; LF, Luyeh fault.

lateral strike-slip component [Angelier *et al.*, 2000] and along-strike variation [Tsai, 1986]. The northernmost portion has a surface slip rate of ~ 1 cm/a [Liu and Yu, 1990; Yu and Kuo, 2001] and a relatively high frequency of large earthquakes, together with a complex stress regime pattern [e.g., Hu *et al.*, 1996; Wu *et al.*, 1997; Kao *et al.*, 1998]. The middle portion has an uplift rate of 1–1.5 cm/a [Liu and Yu, 1990] and low earthquake activity at a shallow depth. The southern portion, from Chihshang to Taitung, is the most active segment along the LVF, and is characterized by a creeping behavior with high slip rate (~ 3 cm/a) and high microseismicity [Liu and Yu, 1990; Angelier *et al.*, 2000; Lee *et al.*, 2003]. The influence of heterogeneous fault

Table 1. Major Events ($M \geq 6$) in the 1951 H–T Sequence

ID in Figure 1	Month/day	Time	M_L
1	10/21	21:34	7.3
2	10/22	03:29	7.1
3	10/22	04:28	6.3
4	10/22	05:18	6.1
5	10/22	05:43	7.1
6	10/22	12:48	6.0
7	10/22	20:52	6.1
8	10/23	01:19	6.1
9	10/23	08:55	6.1
10	11/24	18:47	6.0
11	11/24	18:50	7.3
12	11/26	06:38	6.0

properties on the generation of large earthquakes in eastern Taiwan is a crucial issue for seismic hazard assessment.

[4] Calculation of static Coulomb stress is a powerful tool for explaining the evolution of seismicity patterns [e.g., Harris, 1998; Stein, 1999]. An increase in Coulomb stress change generally corresponds to lobes of off-fault aftershocks [Smith and Van de Lindt, 1969; Das and Scholz, 1981; Stein and Lisowski, 1983; Oppenheimer et al., 1988]. Nevertheless, the static Coulomb stress transfer alone cannot explain the time lag between the main event and triggered events [Harris, 1998; Stein, 1999; Steacy et al., 2005]. The temporal behavior of seismicity has been explained by viscoelastic relaxation [Freed and Lin, 1998, 2001], fault strengthening or weakening [Ito and Matsuzaki, 1990], dynamic stress triggering [Gomberg et al., 2001; Kilb, 2003; Brodsky and Prejean, 2005], pore fluid diffusion [Nur and Booker, 1972; Peltzer et al., 1998], and rate/state friction [Dieterich, 1994]. Recent studies in rate/state stress transfer show encouraging results on large strike-slip fault systems [Dieterich and Kilgore, 1996; Stein et al., 1997; Harris and Simpson, 1998; Toda and Stein, 2003; Toda et al., 2005], offering the prospect of more accurate seismicity forecasting. In the rate/state stress transfer model, the evolution of seismicity depends not only on static stress change, but also on the background seismicity rate, fault stressing rate, and the aftershock decay period [Dieterich, 1994]. This model has been shown to generally agree with the temporal and spatial seismicity in southern California [Toda et al., 2005]. However, the good correlation between seismicity rate and stress triggering was mostly shown in strike-slip fault systems (see reviews by Harris [1998], Stein [1999], and King and Cocco [2000]). Few cases have been examined in thrust systems [e.g., Stein et al., 1994; Wang and Chen, 2001; Lin and Stein, 2004]. The effect of rate/state stress transfer on the space-time aftershock distribution along an oblique fault system remains unclear.

[5] To understand the seismicity evolution in the 1951 H–T sequence, we use a combination of earthquake relocation [Cheng et al., 1996, 1997] and paleoseismic information from re-evaluation of the 1951 surface ruptures [Shyu et al., 2006]. In this study we employ the static Coulomb hypothesis and also look at more complex rate/state friction formulations. We examine if rate/state friction can help us to answer the following questions: (1) What are the controlling factors for the leaping triggered sequence? (2) How does the creeping segment react to the stress change from aftershocks? Our results show that each major rupture of the 1951 H–T sequence occurred in areas of enhanced Coulomb stress, implying that elastic stress transfer can explain the spatial distribution of the major aftershocks but cannot explain the temporal patterns of triggering. Incorporating the rate/state friction into the stress calculation, we offer a physical explanation for why the distant Chihshang fault (characterized by creeping behavior in recent decades) was triggered preferentially.

2. Rupture Model

[6] In order to determine the fault parameters for each fault segment in the 1951 H–T earthquake sequence, we compile focal mechanisms [Cheng et al., 1996] and surface rupture estimates [Hsu, 1962; Shyu et al., 2006]. Given the

surface rupture length reported by Hsu [1962] and Shyu et al. [2006], we use the empirical relation by Wells and Coppersmith [1994] to determine subsurface fault width, length, and slip magnitude of these oblique reverse faults. Earthquake relocation and focal mechanisms reported by Cheng et al. [1996] were used to determine the dip angle, slip direction, and source depth.

[7] The modeled fault planes include four on-land segments (corresponding to Events 1, 10, 11, and 12 in Figure 1 and Table 1) and two offshore segments (Events 2 and 5). For segments with available co-seismic surface rupture estimates (the Chihshang and Yuli segments, re-evaluated by Shyu et al. [2006]), we use the reported surface rupture length (SRL) to re-determine M_w by

$$M_w = 5.00 + 1.22 \cdot \log(\text{SRL}) \quad (1)$$

[Wells and Coppersmith, 1994].

[8] For the segment without observed surface rupture (Taitung segment) and the offshore segments (Events 1, 2, and 5), we use the local magnitude determined by Cheng et al. [1996, 1997] together with the M_w – M_L relation derived from local seismicity [Huang et al., 2000] to obtain M_w .

[9] The subsurface rupture length (RLD) and width (RW) are then calculated by a given M_w using equations (2) and (3):

$$\log \text{RLD} = -2.42 + 0.58M_w \quad (2)$$

[Wells and Coppersmith, 1994];

$$\log \text{RW} = -1.61 + 0.41M_w \quad (3)$$

[Wells and Coppersmith, 1994].

[10] Slip magnitude can be inferred by (slip offset) = $M_o / (\text{shear modulus} \times \text{rupture area})$, where the rupture area is $\text{RLD} \times \text{RW}$ and M_o is seismic moment equivalent to M_w by equation (4).

$$M_o = 10^{1.5(M_w + 10.73)} \quad (4)$$

[Hanks and Kanamori, 1979].

[11] The resolved fault parameters are shown in Table 2.

[12] The depths of the upper and lower edges of the fault are calculated from focal mechanism dip and constrained by rupture area $\text{SRL} \times \text{RW}$. In most cases the top depth is fixed at the surface (0.0 km) because of the very shallow hypocenters (Events 1 and 2), well-defined surface rupture estimates (Events 10 and 11), or location further offshore with large depth uncertainty (Event 5). One exception occurs in Event 12, where the hypocenter depth (49 km) is ~ 20 km below the seismogenic zone, and therefore in this case, we center the fault plane at the hypocenter depth.

3. Coulomb Stress Changes

[13] We calculated the static Coulomb stress changes (ΔCFF) using the above fault parameters for major earthquakes that ruptured in different segments by:

$$\Delta \text{CFF} = \Delta \tau + \mu' \Delta \sigma, \quad (5)$$

Table 2. The 1951 H–T Sequence Source Model

Segment	Representative Event (GMT Time)	ID (Figure 1)	Hypocenters					Focal Mechanisms			Slip, m (shear, reverse)	Length, km	Top, km	Bottom, km
			<i>ML</i>	<i>Mw</i>	lon, deg	lat, deg	depth, km	strike, deg	dip, deg	rake, deg				
Hualien	1951/10/21 21:34	No1	7.3	6.79	121.725	23.875	4	25	85	31	(−1.11, +0.67)	33.06	0	14.89
Hualien	1951/10/22 03:29	No2	7.1	6.60	121.725	24.075	1	25	85	73	(−0.30, +0.99)	25.72	0	23.47
Hualien	1951/10/22 05:43	No5	7.1	6.60	121.950	23.825	18	45	75	60	(−0.52, +0.90)	25.72	0	12.09
Chihshang	1951/11/24 18:47	No10	6.0	6.59	121.225	23.100	16	32	70	70	(−0.35, +0.96)	25.15	0	11.58
Yuli	1951/11/24 18:50	No11	7.3	6.95	121.350	23.275	36	25	70	40	(−0.78, +0.65)	41.08	0	16.38
Taitung	1951/11/26 18:38	No12	6.0	5.40	121.050	22.725	49	8	55	90	(+0.00, +0.25)	5.15	47.35	50.65

where $\Delta\tau$ is the shear stress change along the slip direction on the assumed fault plane, μ' is the apparent coefficient of friction, and $\Delta\sigma$ is the normal stress change. The Coulomb stress changes are calculated at the centers of 1 km \times 1 km cells by the program Coulomb 2.6 [Toda *et al.*, 1998]. Figure 2 shows the effects of varying μ' , dip angle, and rake on stress induced by Event 1. Values of μ' between 0.0 and 0.8 span the range of plausible values (Figures 2a–2c). The dip angle and rake are constrained by the 1951 *M7+* Hualien events (averaged dip-angle and rake are 82° and 55°, respectively) and current *M4+* events in the same area (averaged dip-angle and rake are 62° and 81°, respectively). The range of 60°–90° in dip angle and 50°–80° in rake covers the likely range (see Figures 2d–2i). The sensitivity tests indicate that the Coulomb stress changes caused by the Hualien main shock are sensitive to the rake and dip-angle of a given receiver fault. When the rake increases, the stress increase zone at the north end of the main shock rupture spreads northward; when the dip-angle increases, the on-fault stress increase zone moves closer to the Event 1 fault trace. Despite the different pattern revealed from changing dip-angle and rake, the visual spatial correlation between the next *M7* rupture and stress increase area remains high. The coefficient of friction test in Figures 2a–2c shows that the off-fault Coulomb stress lobes remain the same when μ' is in-between 0.4 and 0.8. A sensitivity test varying μ' , dip-angle, and rake on stress change calculation following the main shock shows that the next rupture plane (Event 5) is located inside the lobe of positive Coulomb stress change (between +0.3 and +2.1 bar) induced by Events 1 and 2. The relationship between the next rupture location and the stress increase zone, therefore, is shown to be insensitive to the selected range of $\mu' = 0.4$ –0.8, dip angle = 60°–90°, and rake = 50°–80°, where the dip angle and rake approximate the minimum and maximum values of the receiver fault models used in the Hualien area.

[14] A sensitivity test on stress induced by Events 1, 2, and 5 on the receiver faults, the Chihshang, Yuli, and Taitung ruptures, is further examined. Ranges of dip-angle and rake are simply selected by $\pm 20^\circ$ of the attitude of the receiver fault, and values of μ' remain between 0.0 and 0.8. By varying μ' , dip angle, and rake in stress change computation, we found that the correlations between sites of

calculated stress increase and locations of the next earthquakes are fairly robust within $\mu' = 0.4$ –0.8 and a variation of 20° with respect to the dip-angle and rake of the receiver fault. These results suggest that the uncertainties in fault parameters are unlikely to cause significant artifacts in the correlation between the subsequent rupture and static stress distribution in this study. Therefore in the following calculation the strike, dip, and rake of each fault model are selected according to the focal mechanisms determined by Cheng *et al.* [1996]. The friction value of 0.4 is selected from the stress transfer study of shallow thrust fault earthquakes by Cochran *et al.* [2004].

[15] The stress evolution at successive rupture sites is illustrated by sequential plots of the Coulomb stress change (Figure 3). Large earthquakes generally relieve stress along the rupture (red zones) and transfer the stress beyond the rupture tips and off the fault (blue zones). We first calculated the static stress changes caused by the *M_L* 7.3 Hualien earthquake on Events 2 and 5 that clustered in the Hualien area (Figures 3a–3b). Figure 3a shows increased Coulomb stress transfer of up to 1 bar at the location of the next event (Event 2). In addition, the events that occurred between the modeled event and next target earthquake (open red circles, hereafter called inter-event aftershocks) are mostly located in the stress increase zone. The combined effect of the main shock and Event 2 on the fault plane of Event 5 is plotted in Figure 3b. Event 5 and half of the inter-event aftershocks are distributed in the negative stress change regions. Considering the 6–8 km location uncertainty at depth for this offshore event [Cheng *et al.*, 1997], we need to examine whether the stress transfer on the solved fault plane changes significantly with target depth. The stress change induced by Events 1 and 2 was re-computed with a range of target depths from 13 to 23 km (Figure 4). We found the stress change in the area between the fault planes of Events 2 and 5 to be very sensitive to the target depth. The correlation between aftershock location and stress increase is better illustrated in Figure 4c when the target depth is deeper. This suggests that depth uncertainty may perhaps explain why Event 5 occurs in the stress shadow in Figure 3b.

[16] The Coulomb stress change caused by the three *M7+* Hualien earthquakes is examined at the hypocentral region of the *M_L* 6.0 Chihshang earthquake (Figure 3c). The

Figure 2. Sensitivity analysis for stress change computation at a depth of 1 km on the Event 2 fault model (dip = 60°, strike = N25°E, rake = 73°) by varying coefficient of friction, dip angle, and rake of the receiver fault. (A–C) The coefficient of friction ranges from 0.0 to 0.8 with the strike, dip, and rake as N25°E, 60°, and 73°E, respectively. (D–F) The dip angle changes from 60° to 90° with the strike, rake, and μ' as N25°E, 73°E, and 0.4, respectively. (G–I) The rake changes from 50° to 80° with the strike, dip angle, and μ' as N25°E, 80°E, and 0.4, respectively.

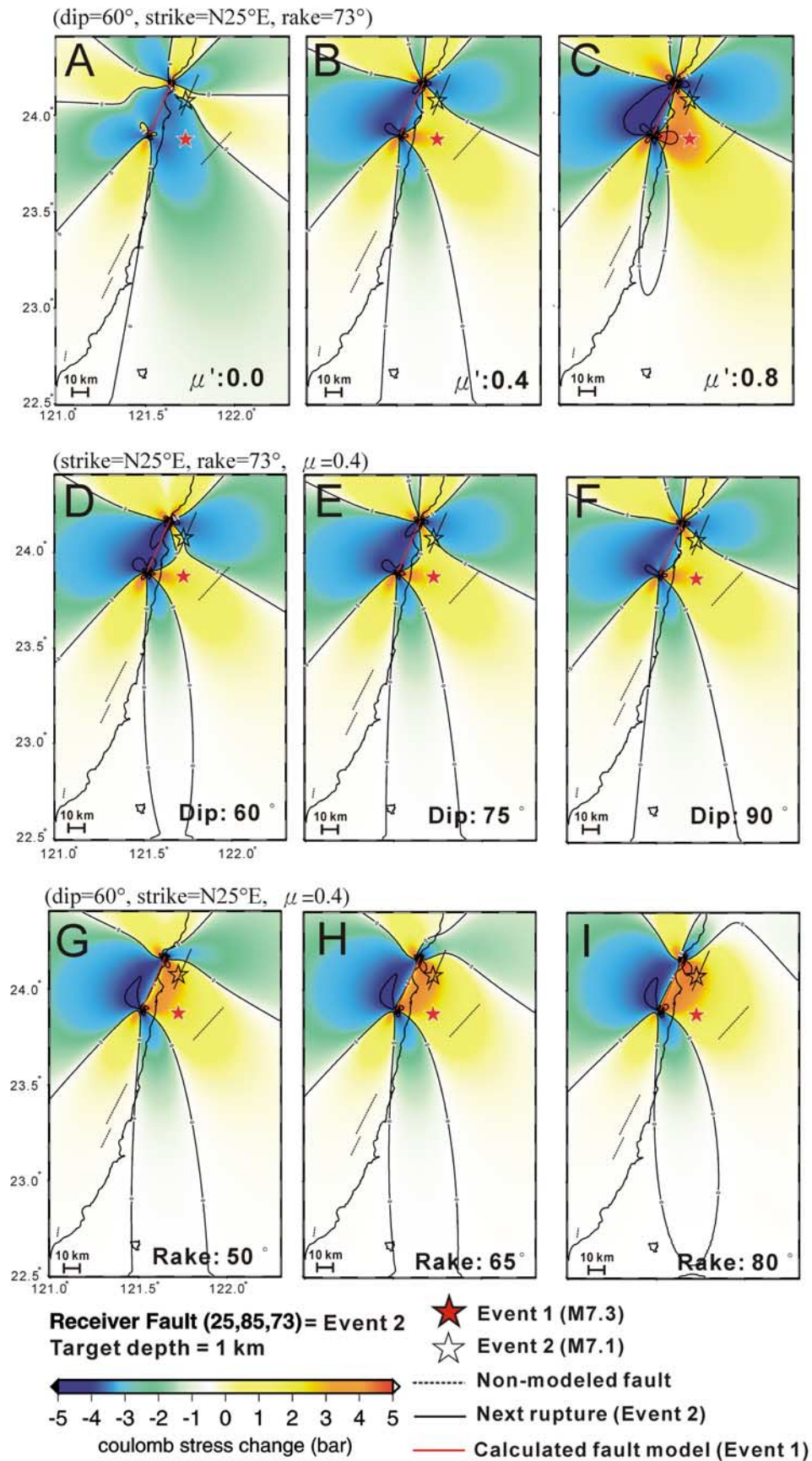


Figure 2

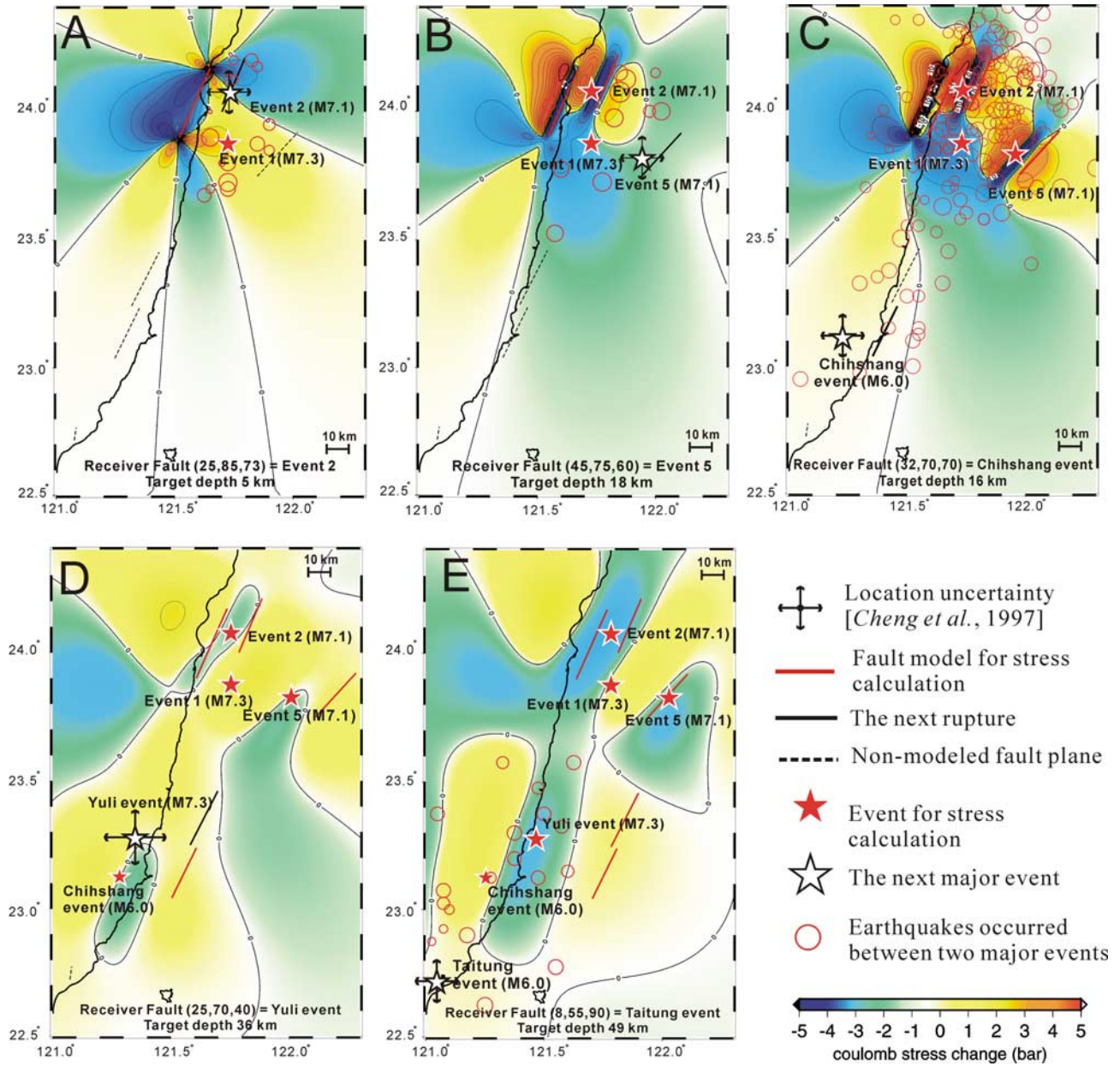


Figure 3. Result of cumulative Coulomb stress changes caused by large earthquakes in the 1951 H–T earthquake sequence. The location uncertainties determined by *Cheng et al.* [1997] are denoted by crosses. Bold red lines denote the surface projections of fault models that are applied to calculate stress state. Bold black lines denote the next surface rupture. Dashed black lines are non-modeled fault planes. Red star shows hypocenter projected at the target depth for stress calculation. Open star shows hypocenter projected at the target depth for the next earthquake to rupture. Red open circle indicates earthquakes that occurred between two major events. Note that target depths are different between the panels according to the depth of the next major event. (a) ΔCFF at a depth of 5 km depth due to the co-seismic displacement of Event 1. Note that the 1 km source depth in Table 2 is too shallow and therefore manually changed to 5 km. Event 1 fault segment is indicated by a bold red line. The relocated epicenters of Event 1 and the next Event 2 are shown by a red star and open black star respectively. (b) ΔCFF at a depth of 18 km due to the co-seismic displacements of Event 1 and Event 2. (c) ΔCFF at a depth of 16 km due to the co-seismic displacements of Events 1, 2, and 5. (d) ΔCFF at a depth of 36 km due to the co-seismic displacements of Events 1, 2, 5, and M_L 6.0 Chihshang earthquake. (e) ΔCFF at a depth of 49 km due to the co-seismic displacements of Events 1, 2, 5, M_L 6.0 Chihshang earthquake, and M_L 7.3 Yuli earthquake.

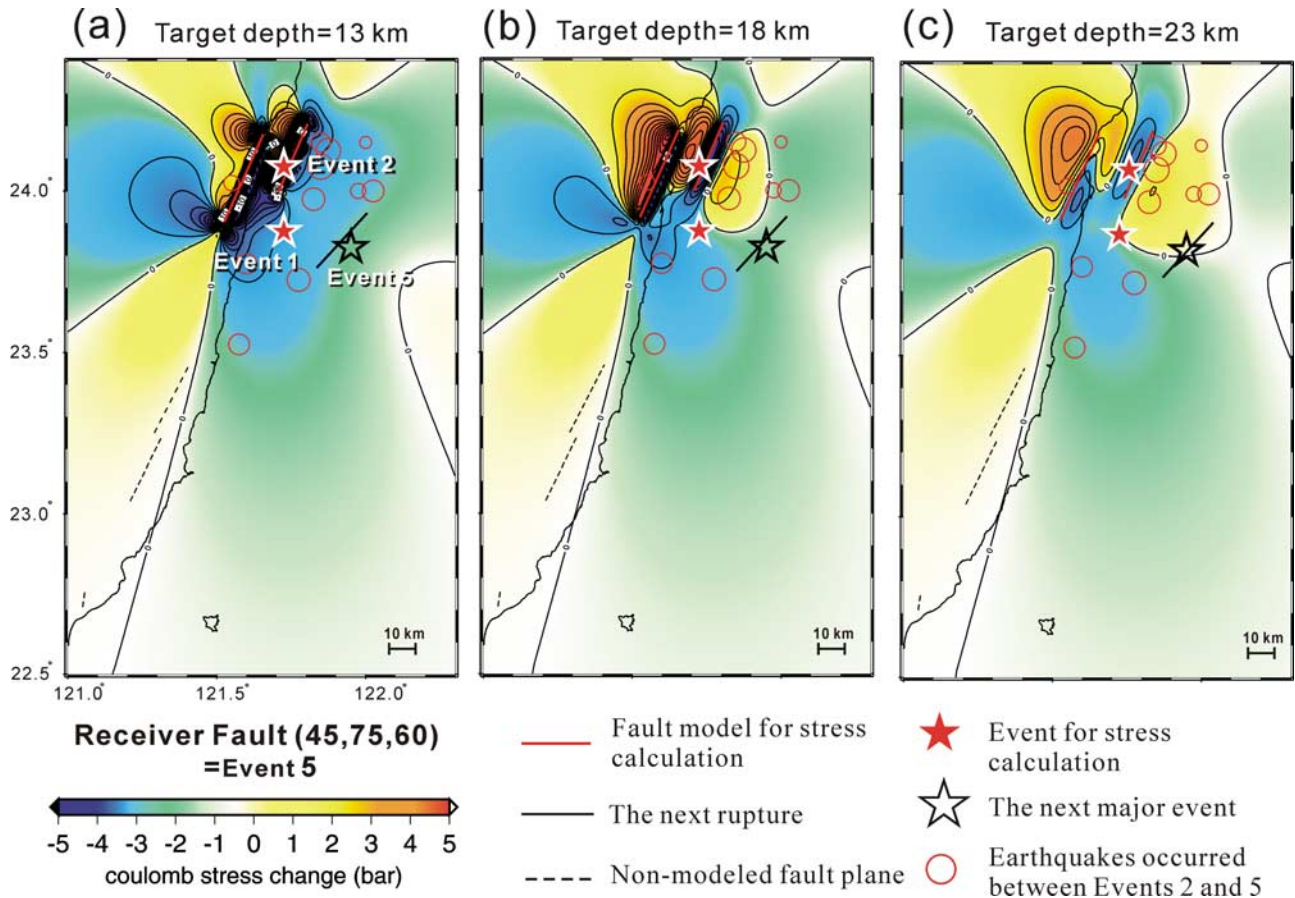


Figure 4. Sensitivity test of stress change calculation to depth uncertainties of Event 5 (furthest offshore). The Coulomb stress change induced by Events 1 and 2 is resolved on the Event 5 fault plane at depths varying from 13 to 23 km.

Coulomb stress is raised by 3–20 bars near the edges of the Hualien rupture zone. Notice that the Chihshang rupture zone (denoted by a bold black line in Figure 3c) lies in a region with 0.14 bar ΔCFF , suggesting that the Hualien earthquakes may have brought the Chihshang fault closer to failure even though the stress magnitude is small. The inter-event aftershocks in Figure 3c are mostly distributed in the zone of positive stress change on the modeled fault plane. It is noteworthy that three $M7+$ Hualien events largely increase the stress in the middle to southern portions of the LVF (Figure 3c), and that the Yuli rupture zone is also located in a positive ΔCFF zone ($\Delta\text{CFF} = 0.2$ bar). This brings into question some temporal features that conventional Coulomb stress hypothesis cannot explain alone. There is clearly a need, therefore, to further involve a temporal dimension in our computation (see section 4).

[17] Figure 3d shows ΔCFF induced by the combined coseismic displacement of the three $M7+$ Hualien events and the M_L 6.0 Chihshang event. The ensuing 40-km rupture of the Yuli fault lies within a region of ΔCFF between 0.3–0.9 bars, and the epicenter of the M_L 7.3 Yuli earthquake occurred in a region where ΔCFF is about 0.7 bar. Thus the Yuli earthquake could have been caused by stress triggering. Figure 3e shows cumulative stress changes computed from the combined coseismic displacements of the three $M7+$ Hualien earthquakes, the M_L 6.0 Chihshang

earthquake, and the M_L 7.3 Yuli earthquake. The Taitung segment (the Luyeh fault) lies within the region of ΔCFF of 0.1 bar, suggesting that the subsequent M_L 6.0 Taitung earthquake was also located in one of the triggered zones. Consequently, regardless of the temporal behavior of triggering, a series of stress calculations indicates that static stress transfer appears to advance slip on the subsequent major earthquake segments in space.

4. Rate/State Friction Model

[18] The static Coulomb stress change calculation cannot explain the temporal triggering effect; therefore we add a temporal dimension to fault friction using the rate/state friction model [Dieterich, 1994]. The “rate” denotes rate at which the fault slips and the “state” indicates the physical properties of the fault surface [Dieterich, 1994]. According to this model, the time-dependent seismicity rate is viewed as a result of a sudden stress step induced by a large earthquake and the time elapsed since the last event; the decay rate depends on fault properties and the loading condition. The seismicity rate (R) at steady state can be written by

$$R = \frac{r}{\gamma \dot{\tau}_r}, \quad (6)$$

where r is the steady state seismicity rate in a region subjected to a shear stressing rate $\dot{\tau}_r$, and γ is a state variable that depends on both time and stress.

[19] When a stress perturbation is present, the state variable γ is controlled by the magnitude of the stress step change; a sudden increase in stress change causes the state variable to drop [e.g., *Toda and Stein*, 2003, equations (4)–(6)]. The state variable changes from γ_{n-1} to a new value γ_n :

$$\gamma_n = \gamma_{n-1} \exp\left(\frac{-\Delta CFF}{A\sigma}\right), \quad (7)$$

where A is a dimensionless fault constitutive parameter (0.005–0.015 from laboratory experiments [*Dieterich*, 1994; *Dieterich and Kilgore*, 1996; *Scholz*, 1998]), σ is the total normal stress, and ΔCFF is the Coulomb stress change induced by an earthquake. The value of $A\sigma$ has been evaluated for different earthquake sequences [*Harris and Simpson*, 1998; *Toda et al.*, 1998; *Stein*, 1999; *Belardinelli et al.*, 2003]. *Dieterich* [1994] notes that the normalized shear stress change ($\Delta\tau/A\sigma$, where $\Delta\tau$ is the stress change induced by an earthquake) is a crucial parameter that scales the magnitude of the spatially dependent stress changes. Here we use $A\sigma = 0.01$ – 0.75 MPa [*Guatteri et al.*, 2001] as the range of values for further sensitivity tests in section 4.3.

[20] After a stress step, the effect of the stress perturbation decreases with time, corresponding to a gradual increase in the state variable. The state variable now changes from γ_n to another new value γ_{n+1} after a time increment of Δt :

$$\gamma_{n+1} = \left[\gamma_n - \frac{1}{\dot{\tau}_r} \right] \exp\left[\frac{-\Delta t \dot{\tau}_r}{A\sigma}\right] + \frac{1}{\dot{\tau}_r}. \quad (8)$$

[21] The shear stressing rate $\dot{\tau}_r$ is generally immeasurable but can be roughly determined using $\dot{\tau}_r = A\sigma/t_a$, where t_a is the aftershock duration.

[22] Equations (7) and (8) show that the state variable at each time step can be determined by the assumed $A\sigma$, the estimates of Coulomb stress change (ΔCFF) and the aftershock duration (t_a). Together with the background seismicity rate estimate (r) in equation (6), the predicted earthquake activity at the time step can also be computed. Consequently, in addition to $A\sigma$, the time-dependent seismicity rate calculation needs three crucial parameters defined: (1) the sudden stress step induced by the major events, (2) the background seismicity rate, and (3) the aftershock duration rate. We know the ΔCFF resolved upon each fault segment (see section 3), but we do not know the r and t_a representative of the fault segments that ruptured in the 1951 H–T sequence. To implement the rate/state model, parameters r and t_a must be specified.

4.1. Background Seismicity Rate

[23] To obtain the background seismicity rate, we start with the available catalogs and search for the most representative seismicity rate model in terms of the catalogs' completeness and accuracy. Figure 5a shows that the 1900–2004 catalog is not uniform in its magnitude of completeness (M_c). The M_c for the 1900–1972 catalog (instrumental seismicity data from the Central Weather Bureau's earlier seismographic network) is 4.75. The M_c for the 1973–1990

catalog from the Taiwan Telemetered Seismographic Network (TTSN) and the 1991–2004 catalog from the Central Weather Bureau Seismic Network (CWBSN) is 2.7 and 2.1 respectively. We obtain a representative pre-1951 $M4+$ background rate by extrapolating from $M4.75+$ rate through the frequency-magnitude distribution. We also calculate the $M4+$ seismicity rate in the 20-year period before the 1999 Chi-Chi earthquake (1979–1999) for comparison.

[24] Considering the large location uncertainties and low detection capability for pre-1951 earthquakes, we determine the background seismicity rate using a $10 \text{ km} \times 10 \text{ km}$ grid. Taking into account only the earthquakes associated with the LVF (see the box in Figure 5b), we plot the along-strike variation of $M4+$ seismicity rate in Figure 5c. The different study periods reveal a consistently high seismicity rate in the Hualien area. Figure 5d shows a quantitative measurement of relative seismicity rates based on the maximum and minimum values in each segment window at different periods, which offers a range of values for further sensitivity analysis in section 4.3. In a given time period, the background rate for each segment is normalized by the Hualien rate. Therefore the Hualien segment seismicity rates are normalized to be 1.

4.2. Aftershock Duration

[25] For a given major earthquake, the aftershock durations (t_a) are determined while the projected aftershock rate decays to the background seismicity, which is independent of main shock magnitude [*Dieterich*, 1994; *Ziv and Rubin*, 2003]. To obtain the aftershock duration for different fault rupture segments, we chose the four largest main shock-aftershock sequences that occurred in the Hualien, Yuli, Chihshang, and Taitung segments individually. The aftershock sequences are selected if they are spatially close to the fault segment of interest and have a $M \geq 6$ main shock (Figure 6). Considering that the aftershock expansion pattern may be strongly associated with fault zone properties [*Tajima and Kanamori*, 1985], we determine the aftershock area using the events that occurred within one month after the main shock (see the dashed ellipse in Figure 6). In the Taitung segment there were no $M \geq 6$ earthquakes between 1973 and 2004, so we choose a $M5$ main shock instead. This $M5$ main shock occurred on 2003/12/18 and was likely triggered by the 2003/12/10 $M6.4$ Chihshang earthquake that was used to estimate the aftershock duration of another segment (the Chihshang segment). However, the aftershock area of the $M5$ Taitung event (dashed ellipse in Figure 6d) is spatially isolated enough from the $M6.4$ Chihshang aftershock (dashed ellipse in Figure 6c), so that we may have an independent measurement of aftershock duration from the Chihshang segment. The selected aftershocks for different segments are then used to plot the earthquake numbers as a function of time (Figure 7). With the estimated background rates prior to the main shock, we can address the decay rate to the background level. As a result, the calculated durations at the Hualien, Yuli, Chihshang, and Taitung segments are 5.5 years, 0.6–1.4 years, 0.22 year, and 0.9–3.3 years respectively.

[26] Considering that the aftershock duration (t_a) is inversely proportional to the stressing rate [*Dieterich*, 1994], and the stressing rate depends on the steady fault slip rates (d) assuming the slip rate is constant in time without

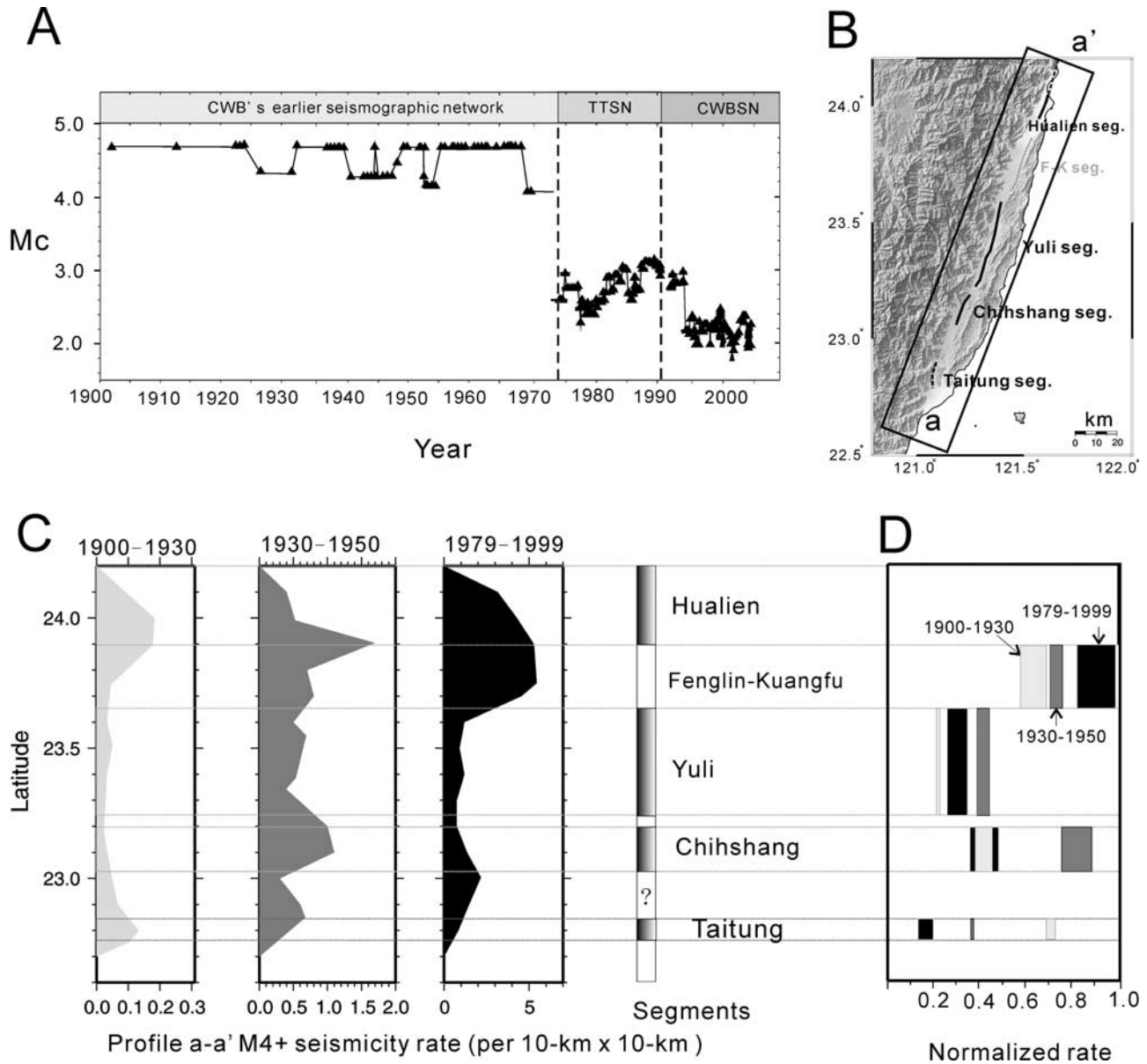


Figure 5. (a) The magnitude of completeness as a function of time. The measurements are separated into three domains with different seismic networks. (b) The study area and the calculation box for along-strike seismicity rate estimates. (c) M_4+ seismicity rate per 100 km² as a function of latitude at different time periods. The bar on the right indicates the fault segmentation from Hsu [1962], where the fault segments of interest are filled with shaded gray. (d) The segmentation of normalized seismicity rate (relative to the Hualien segment) for three different study periods. The rates for 1900–1930 are indicated by light gray boxes. The rates for 1930–1950 and 1979–1999 (prior to the 21 September 1999 Chi-Chi earthquake) are denoted by dark gray and black boxes respectively.

significant stress change induced by surrounding earthquakes taking place, we can write $t_a \propto 1/d$. Here we also use the geodetically derived fault slip rates on the Hualien, Yuli, Chihshang, and Taitung networks [Yu *et al.*, 1990; Loevenbruck *et al.*, 2001] to check whether the above

measurements are reasonable. As shown in Figure 8, the t_a measurement for the Taitung segment does not follow the $t_a - d$ scaling relation determined by the Hualien, Yuli, and Chihshang segments' data. The scaling law leads to $t_a = 12$ years, which shows strong variability compared to the

Figure 6. Four major events representative of different fault segments from north to south. Dashed ellipses encircle the chosen aftershock zones that occurred one month following the main shock for (a) the 20 May 1986 M 6.5 earthquake in Hualien, (b) the 10 June 2003 M 6.5 earthquake near Yuli, (c) the 10 December 2003 M 6.4 earthquake in Chihshang, and (d) the 18 December 2003 M 5.0 earthquake in Taitung.

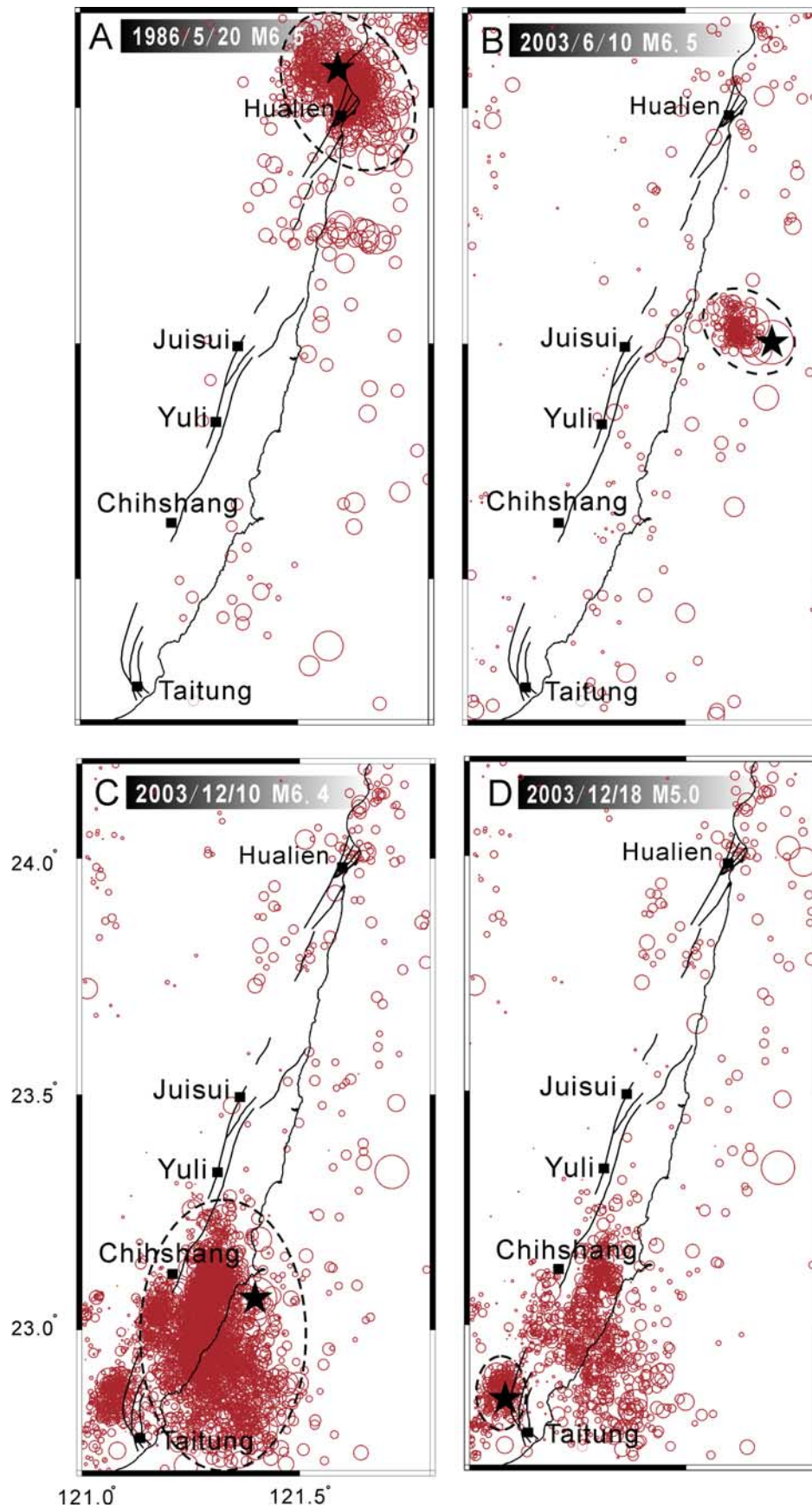


Figure 6

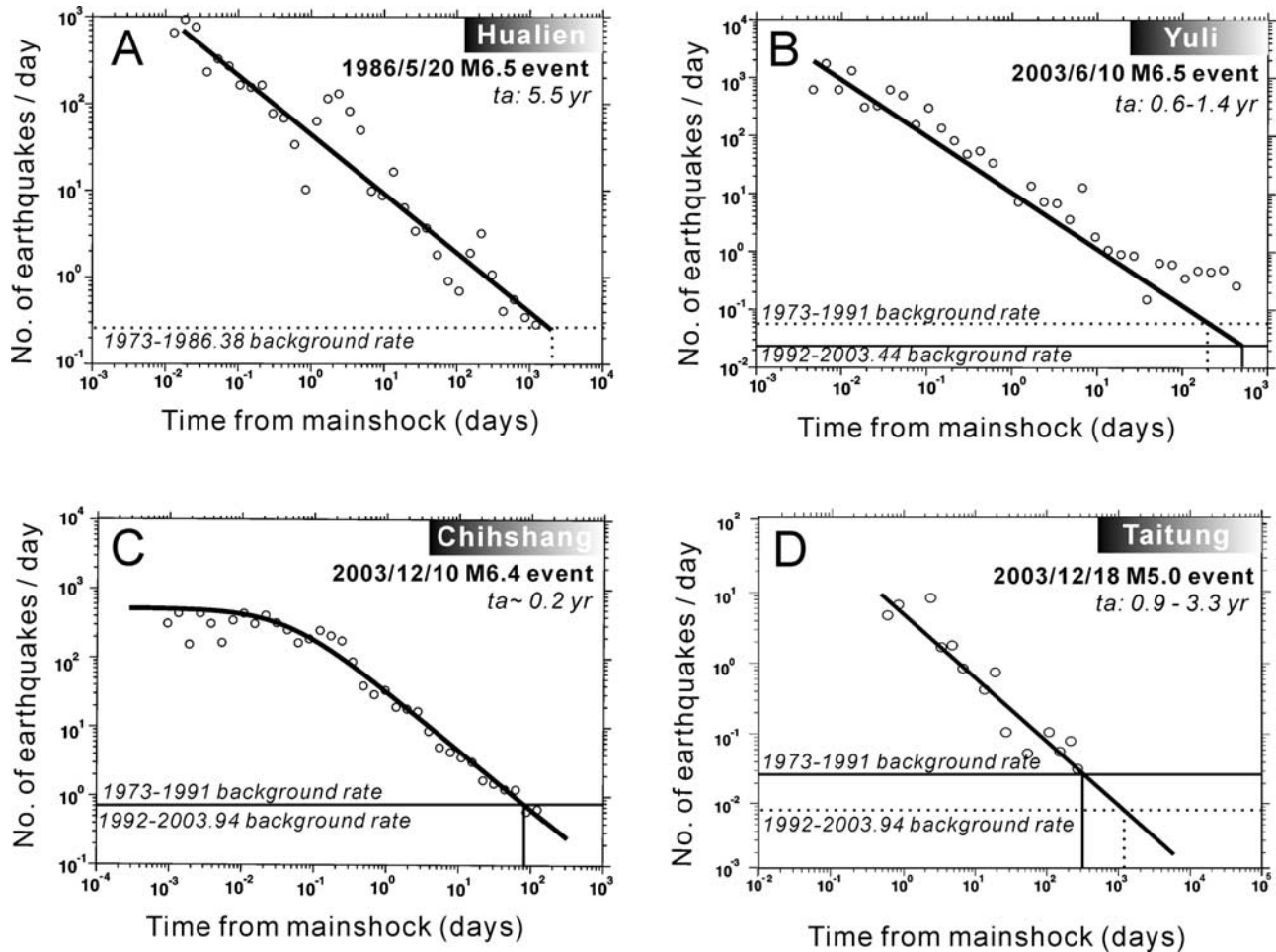


Figure 7. Aftershock rates (open-circles) as a function of time for main shocks on the Hualien segment (a), Yuli segment (b), Chihshang segment (c), and Taitung segment (d), fitted to a modified Omori decay function (solid line). The aftershock durations are obtained when the projected aftershock rates decay to the background seismicity rate. The corresponding locations for the chosen aftershock zones are shown in Figure 6.

values calculated from current seismicity ($t_a = 0.9$ – 3.3 years). We therefore use the wide range of t_a in the Taitung segment, 0.9 – 12 years, for the following computation.

4.3. Results of Predicted Seismicity

[27] The rate/state friction model requires values for the stress change caused by the three $M7+$ Hualien events, the aftershock duration t_a , the seismicity rate, and the combination of normal stress and constitutive constant $A\sigma$ on each receiver fault (i.e., the Yuli, Chihshang, and Taitung segments). A summary of these necessary parameters are shown in Table 3. The 1900–1950 earthquake catalog permits rough estimates of background seismicity rate relative to the Hualien segment (r in Table 3), with the 1979–1999 catalog for a comparison. Regional aftershock durations for large earthquakes were found from the 1991–2004 large earthquake sequences at each fault segment (t_a in Table 3). $A\sigma$ is set to be 0.1 – 7.5 bar [Guatteri et al., 2001]. Using the above choices of aftershock duration, background seismicity rate, $A\sigma$, and the variation of each of these, we determine the expected seismicity rate on the Yuli segment by equations (6)–(8). In Figure 9a, the magnitude of the

sudden increase in the predicted rate changes with the choices of $A\sigma$. For an increase in $A\sigma$, the magnitude of the transient effect declines. In Figure 9b, the starting point of each curve is controlled by background rate estimates (bkg): a higher background rate leads to a higher predicted rate. In Figure 9c, the decay rate of each curve is governed by aftershock duration t_a : larger t_a has slower decay. Note that the range of predicted seismicity rate for different variables is 0.2 – 0.75 in Figure 9a and 9c, and 0.2 – 1.7 in Figure 9b. This suggests that among these variables, background seismicity rate likely plays a significant role on the predicted rate estimate. Therefore we expect the fault segment characterized by a higher background seismicity rate to have higher earthquake productivity over a given time lag.

[28] We next quantitatively compare the predicted rate calculation on each fault segment (Figure 10). In this calculation, we apply the variation of ΔCFF induced by three Hualien $M7+$ shocks at each segment (ΔCFF in Table 3), with three sets of background seismicity rates from different catalogs and a number of choices of $A\sigma$. Note that for the Taitung segment, we consider two extreme choices of

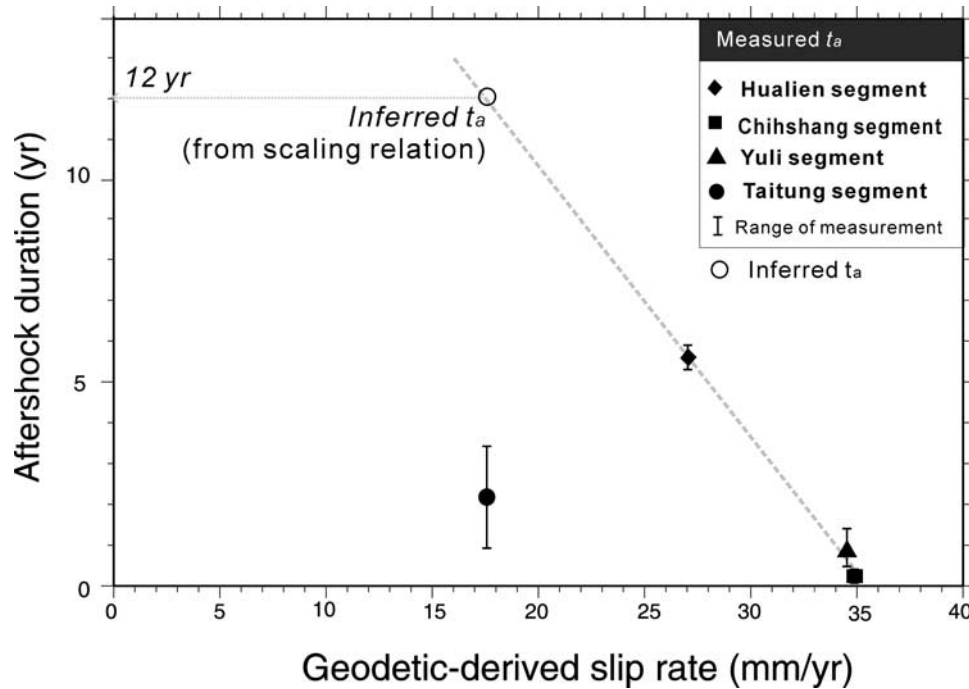


Figure 8. Scaling relations between slip rates on faults and aftershock durations. The filled diamond, square, triangle, and circle represent the observations from the Hualien, Chihshang, Yuli, and Taitung segments respectively. The observed slip rate at the Taitung segment (17.5 mm/a) intersects the regression line to indicate the scaled duration (horizontal dashed arrow). The open circle represents the inferred aftershock duration. The error bars indicate the range of aftershock duration measurements in Figure 7.

t_a , $t_a = 0.9$ years from current seismicity and $t_a = 12$ years from the scaling law. This shows how strong variability in the parameter t_a influences the predicted seismicity rate in the Taitung segment, and how this result affects the order of triggering among segments. As shown in Figures 10a3–10a4, B3–B4, and C3–C4, the aftershock duration that controls the decay rate of the curve likely plays an insignificant role at this timescale (<1.5 months). For a given $A\sigma$ (e.g., $A\sigma = 0.5$), the Chihshang segment has higher earthquake productivity at the time of the next earthquake (34 days after the main shock) due to its higher background seismicity rate in 1930–1950 and 1979–1999. The priority changes from the Chihshang segment to the Taitung segment using the 1900–1930 catalog derived background seismicity rate. Note that the station coverage in eastern Taiwan was improved from 2 stations (before 1930) to 5 stations (1942), and therefore the 1930–1950 catalog offers a somewhat better resolution of seismicity pattern compared to 1900–1930. It also suggests that the uncertainty in the background seismicity rate estimate between segments does exist, which may affect the temporal priority of triggering. Even so, the significance of background seismicity rate on earthquake productivity calculation for the 1951 H–T sequence is clearly seen. We infer that if the Chihshang segment had higher background seismicity rate, as suggested by the 1930–1950 catalog, then it may explain its preceding triggering over the other two segments under the assumption that the sudden stress change, aftershock duration, and background seismicity rate in the rate/state friction

formulation are the major parameters controlling earthquake activity in space and time.

4.4. $M6+$ Probability Model

[29] In the previous section, we showed that the higher earthquake productivity of $M4+$ events predicted from the rate/state stress transfer model leads to the preferential triggering at Chihshang. To further explain the leaping behavior of the 1951 H–T sequence, namely, the order of $M6+$ aftershock triggering, a $M6$ earthquake probability model is needed. Earthquake probability is proportional to the seismicity rate estimate from rate/state friction formulations by

$$P(t, \Delta t) = 1 - \exp\left(-\int_t^{t+\Delta t} R(t) dt\right) \quad (9)$$

where $P(t, \Delta t)$ is the earthquake occurrence probability at the time period t to $t + \Delta t$ and $R(t)$ is the seismicity rate estimate from equations (6)–(8). A higher seismicity rate estimate ($R(t)$) leads to higher earthquake probability ($P(t, \Delta t)$). Under a stationary Poisson model, the probability can be written as

$$P = 1 - \exp(-N), \quad (10)$$

where N is the number of expected earthquakes in a time interval and location of interest.

Table 3. Range of Rate/State Parameters Used in This Study

Parameters	Range			
$A\sigma$	0.1–7.5 bar [Guatteri <i>et al.</i> , 2001]			
r (normalized)	Hualien	Yuli	Chihshang	Taitung
1900–1930	1	0.22–0.23	0.39–0.46	0.69–0.72
1930–1950	1	0.36–0.48	0.75–0.89	0.37–0.38
1979–1999	1	0.25–0.34	0.37–0.48	0.12–0.22
t_a	5.5 yr	0.6–1.4 yr	0.2 yr	0.9–12 yr
ΔCFF (after No.1 event)	×	0.1 bar	0.05 bar	0.01 bar
(After No.2 event)	×	0.3 bar	0.2 bar	0.1 bar
(After No.5 event)	×	0.2 bar	0.14 bar	0.02 bar
(After Chihshang event)	×	0.7 bar	-0.3 bar	0.1 bar

[30] To calculate the time-dependent earthquake probability of a given magnitude, we must know the time-dependent seismicity rate for that magnitude. Given the magnitude-frequency relation [Gutenberg and Richter, 1944] for the earthquake activity at each fault segment, one can transform the expected number of M_4 shocks into the number of M_6 earthquakes by $\log R_{M_6} = \log R_4[(a - b \log 6)/(a - b \log 4)]$, where a is the general earthquake productivity of a volume, and b is the relative size distribution, and R_{M_6} and R_{M_4} are the expected numbers for M_6 and M_4 events per year per volume respectively. The number of M_6 events determined from the above relation may not be precise, but it offers a relative estimate for large earthquake rate in four different segments. Note that we use the 1930–1950 catalog derived seismicity rate for the calculation here (average value for each segment in Figure 5d). Using the estimated M_6 earthquake rate and assumed time interval of 1-year, we compute the 1-year earthquake probability in each 1 km² cell. Figure 11a shows the 1-year earthquake probability for M_6 events. Following the main shock and the two M_7 aftershocks in the Hualien area, the predicted M_6 probability in the Chihshang segment is 2.2–3.1%, which is on average higher than that of Yuli segment (1.5–3.6%) and Taitung segment (0.7–0.9%) considering a wide range of $A\sigma$. Chihshang having the highest probability is consistent with the Chihshang rupture that occurred 34 days after the main shock. After the Chihshang rupture, the M_6 probability in the Yuli segment is predicted to be highest (4.9% in average), which is also consistent with the Yuli rupture that occurred 3 m later (Figure 11b). This shows that the preferential triggering is observed when varying background seismicity rate, after-shock duration, and Coulomb stress change from different fault segments are resolved onto the probability model.

[31] These results, however, depend on the choice of parameters in this study. With the range of Coulomb stress changes (0.01–0.7 bar in this study) and a given $A\sigma$, the predicted M_4 seismicity rate and the M_6 earthquake probability are sensitive to the choices of bkg and t_a . In the stress-based earthquake probability curve (Figure 11a), bkg controls the starting point, and t_a controls the end point. A high bkg together with long t_a lead to a high earthquake probability. Among the fault segments considered, the Chihshang segment is characterized by the shortest t_a and therefore is expected to produce the higher probability due to its high seismicity rate. It is also noted that a small $A\sigma$

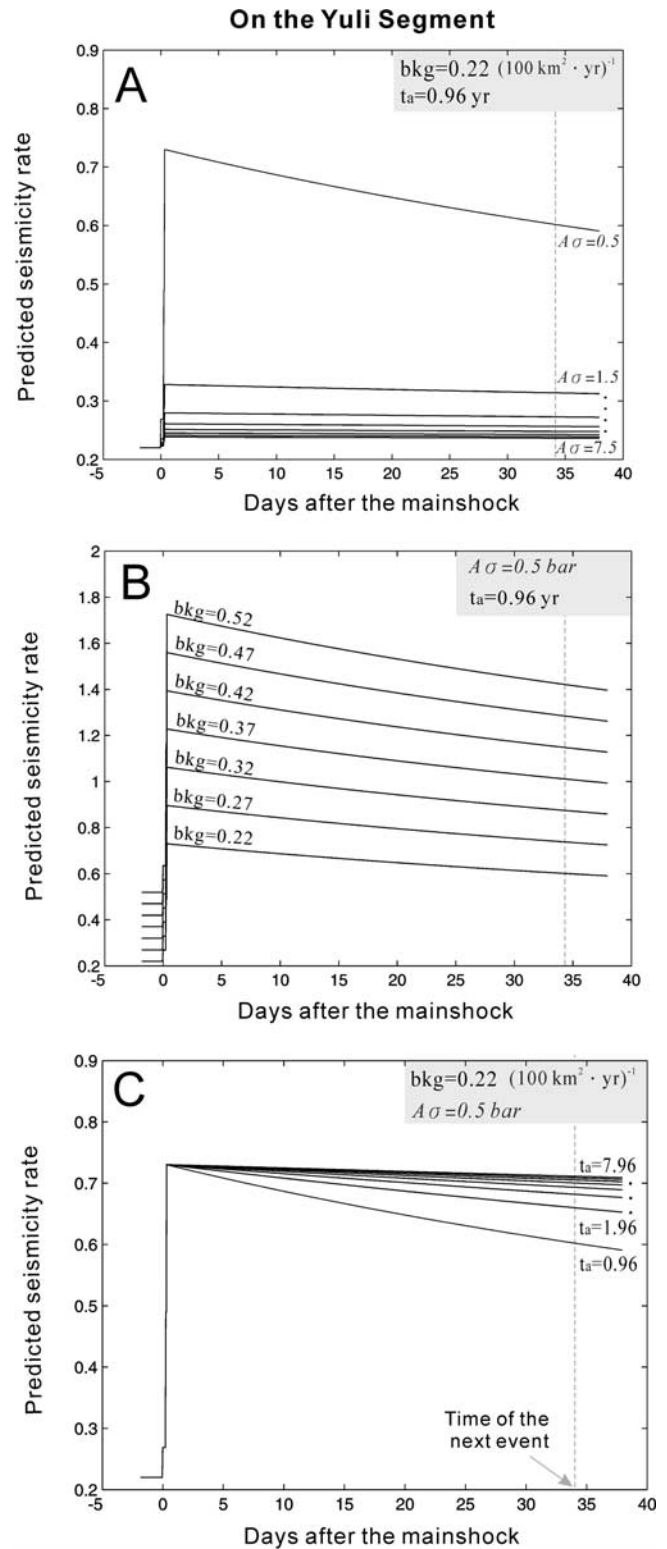


Figure 9. Normalized predicted seismicity rate of the Yuli segment, which ruptured after Event 5. The expected seismicity rate is normalized to the Hualien segment. (a) Time-dependent M_4 rate estimate as a function of $A\sigma$. (b) Time-dependent M_4 rate estimate as a function of background seismicity rate (bkg). (c) Time-dependent M_4 rate estimate as a function of t_a . Vertical dashed line indicates the occurrence of the next M_6 event (the Chihshang event).

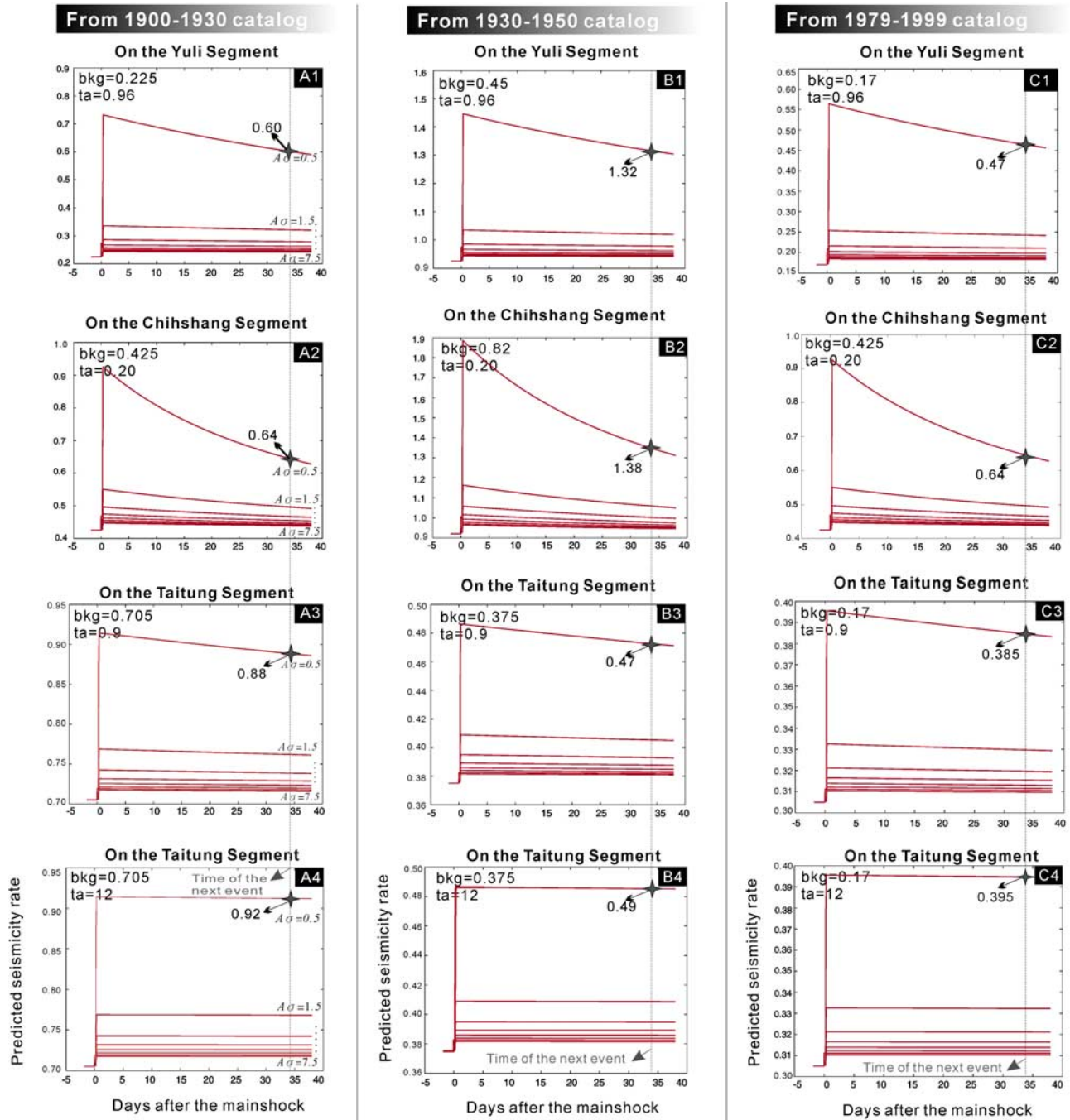


Figure 10. Normalized predicted seismicity rate at each segment that ruptured after Event 5. The seismicity rate is normalized by the Hualien segment. (a) $M4+$ rate estimates using 1900-1930 catalog derived background rate (average value in Figure 5D). (b) $M4+$ rate estimates using the 1930-1950 catalog derived background rate. (c) $M4+$ rate estimates using the 1979-1999 catalog derived background rate. Vertical gray line indicates the occurrence of next $M6$ event (the Chihshang event), gray stars denote the corresponding predicted rate at that time. Two estimates of expected $M4+$ rate in the Taitung segment are determined using different t_a . Required parameters for each case are labeled and shown in Table 3.

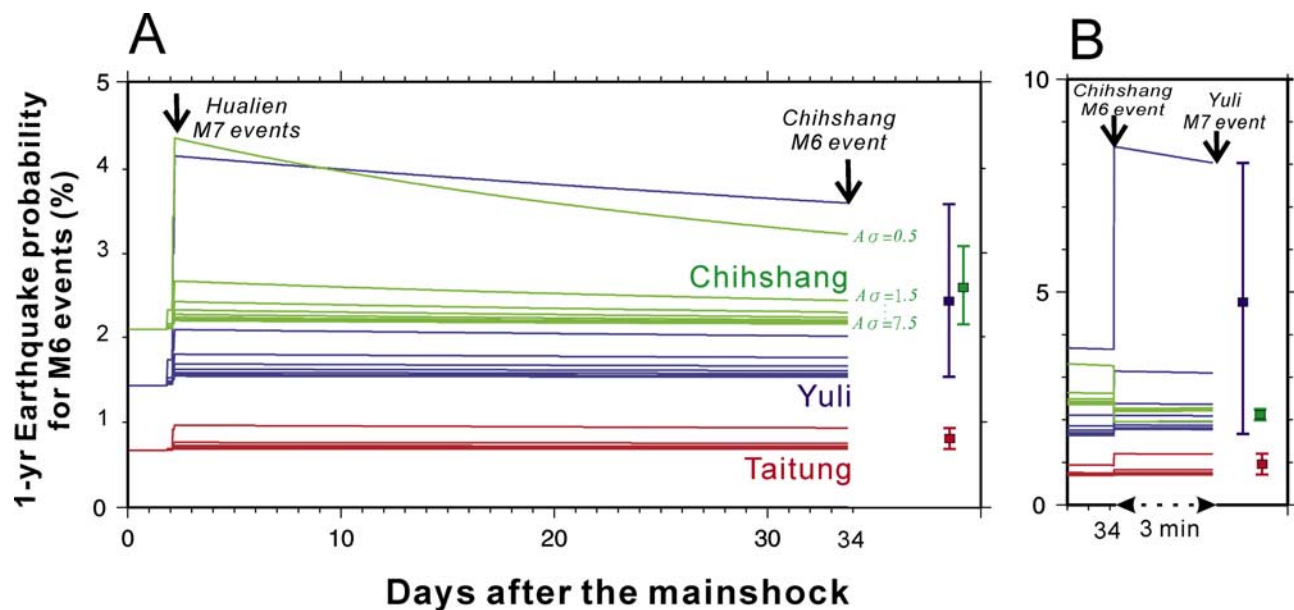


Figure 11. One year probability of $M6+$ earthquakes over the time period (a) between the main shock and the Chihshang event and (b) between the Chihshang event and the Yuli event. The estimates for the Yuli, Chihshang, and Taitung segments are represented by blue, green, and red respectively. Vertical bars indicate the estimates using a wide range of $A\sigma$ with the average denoted by filled squares. Vertical arrows indicate the occurrence of major events of interest in the 1951 H–T sequence.

exaggerates the difference in probability of $M6$ earthquake occurrence between segments, indicating $A\sigma$ likely plays an important role in this model. To improve the earthquake probability model, therefore, further consideration of region-dependent $A\sigma$ is needed.

5. Discussion

5.1. Leaping Behavior Versus Creeping Fault

[32] Is the creeping section always triggered first when a large earthquake occurs far away yet along the same fault system? According to our rate/state modeling result, a faster response toward progressive failure in the creeping section could occur due to 1) smaller but comparable transient effects and 2) the background seismicity rate which is more than twice that of other competitive fault segments. Numerical simulation studies have offered the possible mechanisms: Zöller *et al.* [2005] modeled the characteristics of aftershocks from creeping sections in a heterogeneous fault and suggested that the mean stress in the creeping regions grows rapidly during the main shock and then abates afterward. The high degree of creeping deformation (which depends on the ratio of the creep coefficient between the brittle and creeping sections [Zöller *et al.*, 2005]) leads to the maximum number of aftershocks for several months following the main shock.

5.2. Fault Segmentation

[33] The interplate boundaries capable of generating large earthquakes have been selected for the most focused targets in seismic hazard assessment. It has been suggested that the areas of largest slip release correlate with high b -value regions, and unusually low b -value regions can be regarded as an indication of highly stressed patches in the fault

[Wiemer and Katsumata, 1999; Schorlemmer and Wiemer, 2005]. Aftershock duration also offers a rich source of information about fault segmentation. The duration of the aftershock sequences seems to depend on the nature of the faults, the focal depth, and the stress distribution on the fault. Toda and Stein [2002] examined the aftershock durations in Parkfield, California and found that the aftershock duration in the locked section is eight-fold longer than that in the creeping section. Zöller *et al.* [2005] used a simulation model to show that the high ratio of creep coefficient leads to a fast aftershock decay rate.

[34] Along the LVF, the northernmost segment, Hualien, characterized by the smallest surface slip rate, lowest b -value, and highest seismicity rates, is likely a locked zone with large earthquake potential. In the Chihshang segment, evidence of rapid creeping for at least 20 years [e.g., Yu and Liu, 1989; Angelier *et al.*, 2000; Lee *et al.*, 2001], together with low (less than one year) aftershock duration, seems to agree with the common relation between creeping behavior and relatively short aftershock duration [Toda and Stein, 2002]. The Yuli segment has been seismically inactive in recent decades, and the deep fault behavior of the Yuli fault (i.e., creeping or locked) is still unclear.

[35] During the 1951 H–T sequence, the Yuli segment was characterized by the longest fault rupture and largest co-seismic surface deformation. During the inter-seismic period over the past two decades, the Yuli segment has experienced a similar rapid slip rate of 2–3 cm/a, comparable to that of the creeping Chihshang section [Yu and Kuo, 2001]. However, unlike the abundant background seismicity in the Chihshang area, the Yuli area has been characterized by a much lower seismicity rate during the past few decades (see the 1979–1999 rate in Figure 5). Whether strain energy accumulated in the Yuli segment has been released aseismi-

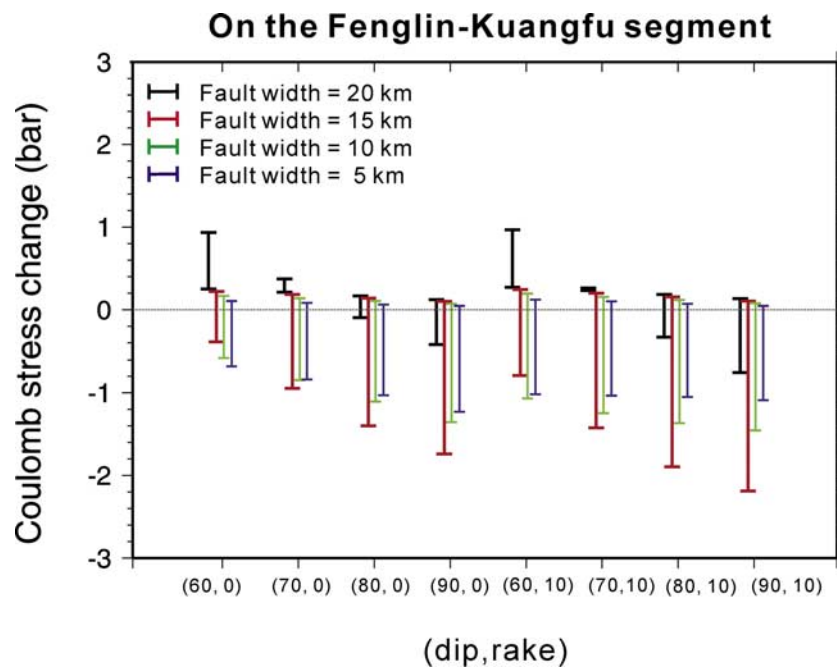


Figure 12. Result of cumulative Coulomb stress changes induced by the Hualien $M7+$ events resolved on the Fenglin-Kuangfu segment with varying dip angles, rakes, and fault widths. Bar denotes the range of calculated Coulomb stress changes. Black, red, green, and blue bars are the results for fault widths 20 km, 15 km, 10 km, and 5 km, respectively.

cally or is building up for the next big earthquake remains a subject of controversy.

[36] We found that the aftershock duration in the Yuli segment is from 0.6 to 1.4 years (see Table 3). *Toda and Stein* [2002] studied the response of the Parkfield-Cholame section of the San Andreas fault to the 1983 Coalinga-Nuñez earthquake, which shows an apparent increase in aftershock duration from 0.6 years in the creeping section to 5 years in the locked section. They pointed out that the limited maximum size of earthquakes in the creeping section probably yields the small aftershock duration. In this study, the $M6$ main shock on the creeping Chihshang fault is calculated to have an aftershock duration of less than one year, which is consistent with the short duration observed in the creeping section along the San Andreas fault. The Yuli segment, characterized by a 0.6–1.5 years aftershock duration, may as well experience aseismic deformation during the past decade. The creeping behavior of the Yuli segment is supported by the inversion result from trilateration and leveling data [Yu *et al.*, 1990; Yu and Kuo, 2001].

[37] The segment between the Hualien and Yuli ruptures, named the Fenglin-Kuangfu segment, has been characterized by intense earthquake activity as shown in Figures 5c and 5d, with predominantly strike-slip faulting [York, 1976]. It is likely a significant fault segment along the LVF, however, did not participate during the 1951 H–T earthquake sequence. To explain the absence of triggering effect on this segment, we compute the Coulomb stress change induced by the Hualien $M7+$ events (Events 1, 2, and 5) on the Fenglin-Kuangfu segment with varying dip angle, rake, and fault width (Figure 12). The range of 60° – 90° in dip angle and 0° – 10° in rake covers the likely range of the $M4+$

event focal mechanisms at the same area. The range of fault width, 5–20 km, is constrained by the focal depths of earthquakes. In Figure 12, the stress changes on the Fenglin-Kuangfu segment are mostly negative despite the applied variations in dip angles, rakes, and fault widths. An exception occurs when the fault width is 20 km, where the stress changes on the Fenglin-Kuangfu segment are averaged to be a positive value. This suggests that under the choice of receiver fault parameters (dip angle = 60° – 90° , rake = 0° – 10° , and width = 0–15 km), the Fenglin-Kuangfu segment is likely located in the stress shadow following the Hualien ruptures, and therefore, is unlikely to be triggered.

5.3. Other Possible Mechanisms for Earthquakes Triggering

[38] The present paper concentrates solely on the concept of static stress transfer; however, other possible triggering mechanisms remain to be discussed. The correlation between observed earthquake propagation patterns and rate/state stress transfer results indicate that the static Coulomb stress changes likely dominate the promotion of large aftershocks in the 1951 H–T sequence. To further support the above statement, the observed geophysical features associated with other triggering mechanisms such as viscoelastic triggering and dynamic stress transfer should be discussed as well. A viscous process is commonly proposed to explain event correlations over large spans of time [e.g., Pollitz *et al.*, 1998; Freed and Lin, 2001]. However, long-delayed triggering is not the specific feature in the 1951 H–T sequence. On the other hand, if dynamic stress triggering is the major mechanism, we ought to see the greatest seismicity rates in line with the directivity following the wave train

[Gomberg *et al.*, 2003]. However, due to the lack of estimates for peak dynamic stresses associated with passing seismic waves for the 1951 H–T sequence, whether dynamic stress transfer contributes to the leaping behavior remains unknown and requires further analysis.

[39] Using the rate/state stress transfer model, the difference in background seismicity rate between segments likely explains the triggering order of the 1951 H–T sequence. However, there is probably more than one mechanism that could have matches for this type of triggering. For example, previous rupture history can lead a given segment near the end of its failure cycle whether background seismicity rate is low or high.

5.4. Spatiotemporal Pattern of Fault Interaction

[40] Faults in different tectonic environments interact in various ways. Spatially, aftershock clusters can occur at significant distance from the main shock. One example of the well known long-distance triggering of large earthquakes is the 1999 $M7.1$ Hector Mine earthquake in California, which occurred 20 km away and 7 years after the 1992 $M7.3$ Landers earthquake [e.g., Gomberg *et al.*, 2001]. Compared with the case in a strike-slip fault system, the time difference between the Hualien and Yuli $M7.3$ earthquakes was 1.5 months over >40 km distance in a thrust fault system, which has a shorter timescale and longer spatial scale of triggering. A comparable example in a dip-slip fault system, Central Nevada, is that the 1954 Fairview Peak ($M7.2$) and Dixie Valley ($M6.8$) earthquakes, showing a few-minute temporal separation over 100 km distance [Caskey and Wesnousky, 1997]. A statistical analysis for 1900–2003 $M > 6.5$ thrust events along the Mexico subduction zone revealed a time difference of a few days to a few years, with few km to >100 km separation [Santoyo *et al.*, 2005]. In all of these cases, stress interaction is the common mechanism responsible [e.g., Caskey and Wesnousky, 1997; Pollitz *et al.*, 2000; Freed and Lin, 2001; Harris and Simpson, 2002; Santoyo *et al.*, 2005]. The above examples in the thrust fault and the subduction zone seemingly reveal the shorter time and longer distance scales of triggering than that in the strike-slip fault system, which is probably related to the typically higher stress changes imparted by thrust faults, as proposed by Lin and Stein [2004]. For the best-documented case, the Landers–Hector Mine earthquake sequence, the most likely mechanism for transmitting post-seismic stresses is viscoelastic relaxation of the lower crust and upper mantle [e.g., Freed and Lin, 2001; Zeng, 2001; Pollitz and Sacks, 2002].

[41] One may argue that the chosen examples for triggering behavior in diverse tectonic environments may not be representative because the fault interaction patterns also depend on the main shock magnitude, rupture histories at neighboring faults, time-dependent fault behavior, and so on. However, it is noted that 35 years after the 1951 H–T sequence (November 1986), a $M7.4$ earthquake shocked the Hualien area again with the $M6+$ aftershocks clustered in the northeastern offshore area of Hualien city. The $M5$ aftershocks propagated southward and followed similar leaping behavior as the 1951 H–T sequence, that is, the $M5$ events occurred on the Chihshang segment a few hours ahead of that on the Yuli segment. This suggests that a common triggering pattern in a given fault system is

possible. Using more worldwide large aftershock data to further examine the existence of region-dependent triggering modes, therefore, is important and useful for improving future estimates of earthquake hazard in the earthquake source areas.

6. Conclusion

[42] Modeling of fault interactions and earthquake triggering during the 1951 $M_L 7.3$ H–T earthquake sequence allows us to understand the temporal patterns of distinct ruptures along the LVF in terms of static stress transfer and rate/state stress transfer models. In the 1951 H–T sequence, the sites of most triggered faults were located where the Coulomb stress was calculated to have increased by the previous event. The conventional static Coulomb stress change due to the $M_L 7.3$ Hualien earthquake, however, cannot explain the temporal triggering behavior where the first off-fault $M6$ aftershock did not occur at the closer fault segment (ΔCFF for the Yuli fault ~ 0.2 bars) but jumped over a long distance (~ 100 km) and ruptured the Chihshang fault ($\Delta CFF \sim 0.14$ bars). Using the static Coulomb stress change coupled with the rate/state stress transfer is probably the correct path to explaining the leaping behavior of faulting along these four distinct faults. Our rate/state stress transfer modeling result implies that the physical properties associated with the high level of seismicity in the Chihshang segment are significantly important for the leaping triggering.

[43] With measurements of the rate/state friction parameters among the different segments along the LVF, we are able to address fault segmentation as a function of time (e.g., along-strike variation of background seismicity rate), which is helpful for further earthquake probability studies in eastern Taiwan. From the short aftershock duration measurement in the Yuli segment, we also suggest that this seismically inactive segment is likely to experience seismic creeping instead of locked behavior with a larger earthquake potential.

[44] **Acknowledgments.** We greatly thank Jyr-Ching Hu and Leslie Hsu for their contributions in improving this manuscript. Also, we are grateful to Roland Bürgmann, J. C. Lee, Bruce Shyu, W. H. Wang, H. T. Chu, and L. H. Chung for helpful discussions on the manuscript. The manuscripts benefited from critical comments from the reviewers Karen Felzer, Jian-Cheng Lee, Ruth Harris, and particularly the Associate Editor Sandy Steacy. This research was supported by the Taiwan Earthquake Research Center (TEC) funded through National Science Council (NSC) with grant 95-2119-M-006-002. TEC contribution number 00014.

References

- Abe, K. (1981), Magnitudes of large shallow earthquakes from 1904 to 1980, *Phys. Earth Planet. Inter.*, 27, 72–92.
- Angelier, J., H. T. Chu, J. C. Lee, and J. C. Hu (2000), Active faulting and earthquake hazard: The case study of the Chihshang Fault, Taiwan, *J. Geodyn.*, 29, 151–185.
- Belardinelli, M. E., A. Bizzarri, and M. Cocco (2003), Earthquake triggering by static and dynamic stress changes, *J. Geophys. Res.*, 108(B3), 2135, doi:10.1029/2002JB001779.
- Brodsky, E. E., and S. G. Prejean (2005), New constraints on mechanisms of remotely triggering seismicity at Long Valley Caldera, *J. Geophys. Res.*, 110, B04302, doi:10.1029/2004JB003211.
- Caskey, S. J., and S. G. Wesnousky (1997), Static stress changes and earthquake triggering during the 1954 Fairview Peak and Dixie Valley earthquakes, central Nevada, *Bull. Seismol. Soc. Am.*, 87(3), 521–527.
- Cheng, S. N., Y. T. Yeh, and M. D. Yu (1996), The 1951 Taitung earthquake in Taiwan, *J. Geol. Soc. China*, 39(3), 267–285.

- Cheng, S. N., T. T. Yu, Y. T. Yeh, and Z. S. Chang (1997), Relocation of the 1951 Hualien, Taitung earthquake sequence, in *Proceedings of Meteorology, Conference on Weather Analysis and Forecasting*, pp. 690–699, Central Weather Bureau, Taipei, Taiwan.
- Cochran, E. S., J. E. Vidale, and S. Tanaka (2004), Earth tides can trigger shallow thrust fault earthquakes, *Science*, *306*, 1164–1166.
- Das, S., and C. H. Scholz (1981), Theory of time-dependent rupture in the Earth, *J. Geophys. Res.*, *86*, 6039–6051.
- Dieterich, J. H. (1994), A constitutive law for rate of earthquake production and its application to earthquake clustering, *J. Geophys. Res.*, *99*, 2601–2618.
- Dieterich, J. H., and B. Kilgore (1996), Implications of fault constitutive properties for earthquake prediction, *Proc. Natl. Acad. Sci. U.S.A.*, *93*, 3787–3794.
- Freed, A. M., and J. Lin (1998), Time-dependent changes in failure stress following thrust earthquakes, *J. Geophys. Res.*, *103*, 24,393–24,409.
- Freed, A. M., and J. Lin (2001), Delayed triggering of the 1999 Hector Mine earthquake by viscoelastic stress transfer, *Nature*, *411*, 180–183.
- Gomberg, J., P. A. Reasenberg, P. Bodin, and R. A. Harris (2001), Earthquake triggering by seismic waves following the Landers and Hector Mine earthquakes, *Nature*, *411*, 462–466.
- Gomberg, J., P. Bodin, and P. A. Reasenberg (2003), Observation earthquakes triggered in the near field by dynamic deformations, *Bull. Seismol. Soc. Am.*, *93*, 118–138.
- Guatterli, M., P. Spudich, and G. C. Beroza (2001), Inferring rate and state friction parameters from a rupture model of the 1995 Hyogo-ken Nanbu (Kobe) Japan earthquake, *J. Geophys. Res.*, *106*(B11), 26,511–26,521.
- Gutenberg, R., and C. F. Richter (1944), Frequency of earthquake in California, *Bull. Seismol. Soc. Am.*, *34*, 185–188.
- Gutenberg, R., and C. F. Richter (1954), *Seismicity of the Earth and associated phenomena*, 2nd ed., 310 pp., Princeton University Press, Princeton, New Jersey.
- Harris, R. A. (1998), Introduction to special section: Stress triggers, stress shadows, and implications for seismic hazard, *J. Geophys. Res.*, *103*, 24,347–24,358.
- Harris, R. A., and R. W. Simpson (1998), Suppression of large earthquakes by stress shadows: A comparison of Coulomb and rate-and-state failure, *J. Geophys. Res.*, *103*, 24,439–24,452.
- Harris, R. A., and R. W. Simpson (2002), The 1999 Mw7.1 Hector Mine, California earthquake - A test of the stress shadow hypothesis?, *Bull. Seismol. Soc. Am.*, *92*(4), 1497–1512.
- Hanks, T. C., and H. Kanamori (1979), A moment magnitude scale, *J. Geophys. Res.*, *84*, 2348–2350.
- Hsu, T. L. (1962), Recent faulting in the Longitudinal Valley of eastern Taiwan, *Mem. Geol. Soc. China*, *1*, 95–102.
- Hsu, H. F. (1985), Analyzing the crustal movement and structure in eastern Taiwan from trilateration networks measurements, *Geodetic Eng.*, *27*(1), 1–10, in Chinese.
- Hu, J. C., J. Angelier, J. C. Lee, H. Y. Chu, and D. Byrne (1996), Kinematics of convergence, deformation and stress distribution on the Taiwan collision area: 2-D finite-element numerical modeling, *Tectonophysics*, *255*, 243–268.
- Huang, K. C., H. Kao, and Y. M. Wu (2000), The determination of M_L - M_w in Taiwan, *8th Annual Meeting of Geophysical Society of China*, 193–201. (in Chinese).
- Ito, K., and M. Matsuzaki (1990), Earthquakes as self-organized critical phenomena, *J. Geophys. Res.*, *95*, 6853–6860.
- Kao, H., P. R. Jian, K. F. Ma, B. S. Huang, and C. C. Liu (1998), Moment-tensor inversion for offshore earthquake east of Taiwan and their implications to regional collision, *Geophys. Res. Lett.*, *25*(19), 3619–3622.
- Kilb, D. (2003), A strong correlation between induced peak dynamic Coulomb stress change from the 1992 M7.3 Landers earthquake and the hypocenter of the 1999 M7.1 Hector Mine earthquake, *J. Geophys. Res.*, *108*(B1), 2003, doi:10.1029/2001JB000678.
- King, G. C. P., and M. Cocco (2000), Fault interaction by elastic stress changes: New clues from earthquake sequences, *Adv. Geophys.*, *44*, 1–36.
- Lee, W. H. K., F. T. Wu, and S. C. Wang (1978), A catalog of instrumentally determined earthquakes in China (magnitude 6 and larger) compiled from various sources, *Bull. Seismol. Soc. Am.*, *68*, 383–398.
- Lee, J. C., J. Angelier, H. T. Chu, J. C. Hu, and F. S. Jeng (2001), Continuous monitoring of an active fault in a plate suture zone: A creepmeter study of the Chihshang Fault, eastern Taiwan, *Tectonophysics*, *333*, 219–240.
- Lee, J. C., J. Angelier, H. T. Chu, J. C. Hu, F. S. Jeng, and R. J. Rau (2003), Active fault creep variations at Chihshang, Taiwan, revealed by creep meter monitoring, 1998–2001, *J. Geophys. Res.*, *108*(B1), 2528, doi:10.1029/2003JB002394.
- Lin, J., and R. S. Stein (2004), Stress triggering in thrust and subduction earthquakes and stress interaction between the southern San Andreas and nearby thrust and strike-slip faults, *J. Geophys. Res.*, *109*, B02303, doi:10.1029/2003JB002607.
- Liu, C. C., and S. B. Yu (1990), Vertical crustal movements in eastern Taiwan and their tectonic implications, *Tectonophysics*, *183*, 111–119.
- Loevenbruck, A., X. Le Pichon, R. Cattin, M. L. Courty, and S. B. Yu (2001), Seismic cycle in Taiwan derived from GPS measurements, *Acad. Sci.*, *333*, 57–64.
- Nur, A., and J. Booker (1972), Aftershocks caused by pore fluid flow?, *Science*, *175*, 885–887.
- Oppenheimer, D. H., P. A. Reasenberg, and R. W. Simpson (1988), Fault plane solutions for the 1984 Morgan Hill, California, earthquake sequence: Evidence for the state of stress on the Calaveras fault, *J. Geophys. Res.*, *93*, 9007–9026.
- Peltzer, G., P. Rosen, F. Rogez, and K. Hudnut (1998), Poroelastic rebound along the Landers 1992 earthquake surface rupture, *J. Geophys. Res.*, *103*(B12), 30,131–30,145.
- Pollitz, F. F., and I. S. Sacks (2002), Stress triggering of the 1999 Hector Mine earthquake by transient deformation following the 1992 Landers earthquake, *Bull. Seismol. Soc. Am.*, *92*(4), 1487–1496.
- Pollitz, F. F., R. Bürgmann, and B. Romanowicz (1998), Viscosity of oceanic asthenosphere inferred from remote triggering of earthquakes, *Science*, *280*, 1245–1249.
- Pollitz, F. F., G. Peltzer, and R. Bürgmann (2000), Mobility of continental mantle: Evidence from postseismic geodetic observations following the 1992 Landers earthquake, *J. Geophys. Res.*, *105*, 8035–8054.
- Santoyo, M. A., S. K. Singh, T. Mikumo, and M. Ordaz (2005), Space-time clustering of large thrust earthquakes along the Mexican subduction zone: An evidence of source stress interaction, *Bull. Seismol. Soc. Am.*, *95*(5), 1856–1864.
- Scholz, C. H. (1998), Earthquakes and friction laws, *Nature*, *391*, 37–42.
- Schorlemmer, D. and S. Wiemer (2005), Microseismicity data forecast rupture area, *Nature*, *434*, 1086.
- Shyu, J. B. H., L. H. Chung, Y. G. Chen, J. C. Lee, and K. Sieh (2006), Re-evaluation of the surface ruptures of the November 1951 earthquake series in eastern Taiwan, and its neotectonic implications, *J. Asian Earth Sci.*, doi:10.016/j.jseas.2006.07.018.
- Smith, S. W., and W. Van de Lindt (1969), Strain adjustments associated with earthquakes in southern California, *Bull. Seismol. Soc. Am.*, *59*(4), 1569–1589.
- Steacy, S., J. Gomberg, and M. Cocco (2005), Introduction to special section: Stress transfer, earthquake triggering, and time-dependent seismic hazard, *J. Geophys. Res.*, *110*, B05S01, doi:10.1029/2005JB003692.
- Stein, R. S. (1999), The role of stress transfer in earthquake occurrence, *Nature*, *402*, 605–609.
- Stein, R. S., and M. Lisowski (1983), The 1979 Homestead Valley earthquake sequence, California: Control of aftershock and postseismic deformation, *J. Geophys. Res.*, *88*, 6477–6490.
- Stein, R. S., G. C. P. King, and J. Lin (1994), Stress triggering of the 1994 $M = 6.7$ Northridge, California, earthquake by its predecessors, *Science*, *265*, 1432–1435.
- Stein, R. S., A. A. Barka, and J. H. Dieterich (1997), Progressive failure on the North Anatolian fault since 1939 by earthquake stress triggering, *Geophys. J. Int.*, *128*, 594–604.
- Taiwan Weather Bureau (1952), *The 1951 earthquake report*, 83 pp., Taiwan Weather Bureau, Taipei (in Chinese).
- Tajima, F., and H. Kanamori (1985), Global survey of aftershock area expansion patterns, *Phys. Earth Planet. Inter.*, *40*, 77–134.
- Toda, S., and R. S. Stein (2002), Response of the San Andreas Fault to the 1983 Coalinga-Nuñez Earthquakes: An application of interaction-based probabilities for Parkfield, *J. Geophys. Res.*, *107*(B6), 2126, doi:10.1029/2001JB000172.
- Toda, S., and R. S. Stein (2003), Toggling of seismicity by the 1997 Kagoshima earthquake couplet: A demonstrating of time-dependent stress transfer, *J. Geophys. Res.*, *108*(B12), 2567, doi:10.1029/2003JB002527.
- Toda, S., R. S. Stein, P. A. Reasenberg, and J. H. Dieterich (1998), Stress transferred by the $M_w = 6.9$ Kobe, Japan, shock: Effect on aftershocks and future earthquake probabilities, *J. Geophys. Res.*, *103*, 24,543–24,565.
- Toda, S., R. S. Stein, K. Richards-Dinger, and S. Bozkurt (2005), Forecasting the evolution of seismicity in southern California: Animations built on earthquake stress transfer, *J. Geophys. Res.*, *110*, B05S16, doi:10.1029/2004JB003415.
- Tsai, Y. B. (1986), Seismotectonics of Taiwan, *Tectonophysics*, *125*, 17–37.
- Wang, W. H., and C. H. Chen (2001), Static stress transferred by the 1999 Chi-Chi, Taiwan, earthquake: Effects on the stability of the surrounding fault systems and aftershock triggering with a 3D fault-slip model, *Bull. Seismol. Soc. Am.*, *91*, 1041–1052.
- Wells, D. L., and K. J. Coppersmith (1994), New empirical relationships among magnitude, rupture length, rupture width, rupture area, and surface displacement, *Bull. Seismol. Soc. Am.*, *84*, 974–1002.

- Wiemer, S., and K. Katsumata (1999), Spatial variability of seismicity parameters in aftershock zones, *J. Geophys. Res.*, *104*, 13,135–13,151.
- Wu, F. T., R. J. Rau, and D. Salzberg (1997), Taiwan orogeny: Thin-skinned or lithospheric collision, *Tectonophysics*, *274*, 191–220.
- York, J. E. (1976), Quaternary faulting in eastern Taiwan, *Bull. Geol. Surv. Taiwan*, *25*, 63–75.
- Yu, S. B., and C. C. Liu (1989), Fault creep on the central segment of the Longitudinal Valley Fault, eastern Taiwan, *Proc. Geol. Soc. China*, *32*(3), 209–231.
- Yu, S. B., and L. C. Kuo (2001), Present-day crustal motion along the Longitudinal Valley Fault, eastern Taiwan, *Tectonophysics*, *333*, 199–217.
- Yu, S. B., D. D. Jackson, G. K. Yu, and C. C. Liu (1990), Dislocation model for crustal deformation in the longitudinal valley area, eastern Taiwan, *Tectonophysics*, *183*, 97–109.
- Zeng, Y. H. (2001), Viscoelastic stress-triggering of the 1999 Hector Mine earthquake by the 1992 Landers earthquake, *J. Geophys. Res.*, *105*, 13,631–13,642.
- Ziv, A., and A. M. Rubin (2003), Implications of rate-and-state friction for properties of aftershock sequence: Quasi-static inherently discrete simulations, *J. Geophys. Res.*, *108*(B1), 2051, doi:10.1029/2001JB001219.
- Zöller, G., S. Hainzl, M. Holschneider, and Y. Ben-Zion (2005), Aftershocks resulting from creeping sections in a heterogeneous fault, *Geophys. Res. Lett.*, *32*, L03308, doi:10.1029/2004GL021871.
-
- K. H. Chen and R.-J. Rau, Department of Earth Sciences, National Cheng Kung University, Tainan, Taiwan. (raurj@mail.ncku.edu.tw)
- S. Toda, Active Fault Research Center, Geological Survey of Japan, National Institute of Advanced Industrial Science and Technology, Tsukuba, Japan.